JACS
JOURNAL OF THE AMERICAN CHEMICAL SOCIETY
pubs.acs.org/JACS
Article

Py-Macrodipa: A Janus Chelator Capable of Binding Medicinally Relevant Rare-Earth Radiometals of Disparate Sizes

Aohan Hu, Eduardo Aluicio-Sarduy, Victoria Brown, Samantha N. MacMillan, Kaelyn V. Becker, Todd E. Barnhart, Valery Radchenko, Caterina F. Ramogida, Jonathan W. Engle, and Justin J. Wilson*

Cite This: J. Am. Chem. Soc. 2021, 143, 10429–10440
Read Online
ACCESS | Metrics & More | Article Recommendations | Supporting Information

ABSTRACT: Nuclear medicine leverages different types of radiometals for disease diagnosis and treatment, but these applications usually require them to be stably chelated. Given the often-disparate chemical properties of these radionuclides, it is challenging to find a single chelator that binds all of them effectively. Toward addressing this problem, we recently reported a macrocyclic chelator macrodipa with an unprecedented "dual-size-selectivity" pattern for lanthanide (Ln^{3+}) ions, characterized by its high affinity for both the large and the small Ln^{3+} (*J. Am. Chem. Soc*, **2020**, *142*, 13500). Here, we describe a second-generation "macrodipa-type" ligand, py-macrodipa. Its coordination chemistry with Ln^{3+} was thoroughly investigated experimentally and computationally. These studies reveal that the Ln^{3+}–py-macrodipa complexes exhibit enhanced thermodynamic and kinetic stabilities compared to Ln^{3+}–macrodipa, while retaining the unusual dual-size selectivity. Nuclear medicine applications of py-macrodipa for chelating radiometals with disparate chemical properties were assessed using the therapeutic $^{135}La^{3+}$ and diagnostic $^{44}Sc^{3+}$ radiometals representing the two size extremes within the rare-earth series. Radiolabeling and stability studies demonstrate that the rapidly formed complexes of these radionuclides with py-macrodipa are highly stable in human serum. Thus, in contrast to gold standard chelators like DOTA and macropa, py-macrodipa can be harnessed for the simultaneous, efficient binding of radiometals with disparate ionic radii like La^{3+} and Sc^{3+}, signifying a substantial achievement in nuclear medicine. This concept could enable the facile incorporation of a breadth of medicinally relevant radiometals into chemically identical radiopharmaceutical agents. The fundamental coordination chemistry learned from py-macrodipa provides valuable insight for future chelator development.

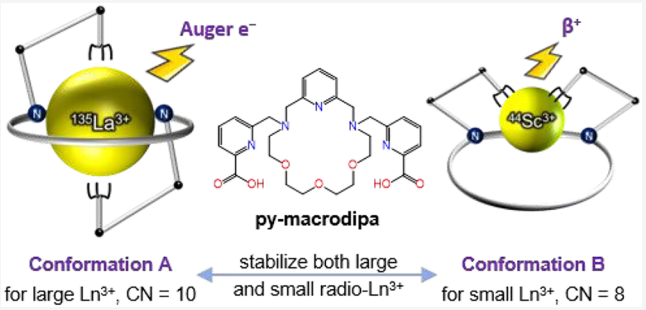

INTRODUCTION

Nuclear medicine is a rapidly growing and critically important branch of radiology that uses radionuclides to diagnose and treat diseases.[1−4] Radionuclides that are suitable for different applications within nuclear medicine are chosen based on their radioactive emission properties and physical half-lives. On the basis of these criteria, nearly the entire periodic table is represented by elements with potential relevance in nuclear medicine.[5−9] As such, the chemical properties of these radionuclides can vary widely, requiring different strategies for making them into radiopharmaceutical agents. For metallic radionuclides, their incorporation into useful therapeutic and diagnostic moieties requires the use of a chelator. These chelators need to be designed and optimized to rapidly and efficiently bind to the desired radiometal and form stable coordination compounds that remain intact in vivo.[10] The chelators that have been used in clinically approved metal-based radiopharmaceutical agents are all derivatives of two structures, 1,4,7,10-tetraazacyclododecane-1,4,7,10-tetraacetic acid (DOTA, Chart 1)[11] and diethylenetriaminepentaacetic acid (DTPA, Chart 1). Although both chelators are highly effective for many smaller ions, like Lu^{3+} and In^{3+}, they are insufficient for use with larger ions. As such, new chelators are needed for medicinally valuable radionuclides with different chemical properties.

A key challenge in this area has been to design ligands that are effective for very large metal ions. Due to their more diffuse charge density and steric requirements, the chelation of large metal ions is typically inefficient with the conventional chelators DOTA and DTPA, thus driving a need for more suitable analogues. In this context, the ligand macropa or bp18c6 (Scheme 1), which possesses an unusual selectivity for larger lanthanide (Ln^{3+}) ions over smaller ones (Table 1),[12] has arisen as a promising candidate. This chelator has shown particular value for its ability to chelate and stably retain large

Received: May 24, 2021
Published: June 30, 2021

Chart 1. Structures of Ligands Discussed in This Work

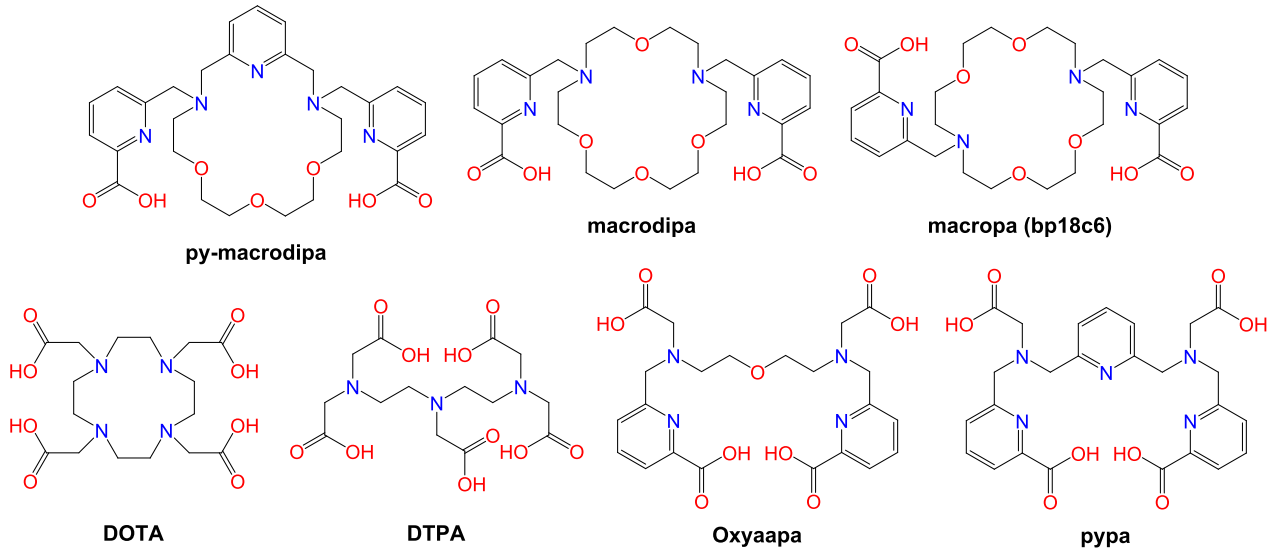

Scheme 1. Depiction of the Conformational Toggle Present in "Macrodipa-Type" Ligands when Chelating Ln^{3+} Ions with Different Sizes[a]

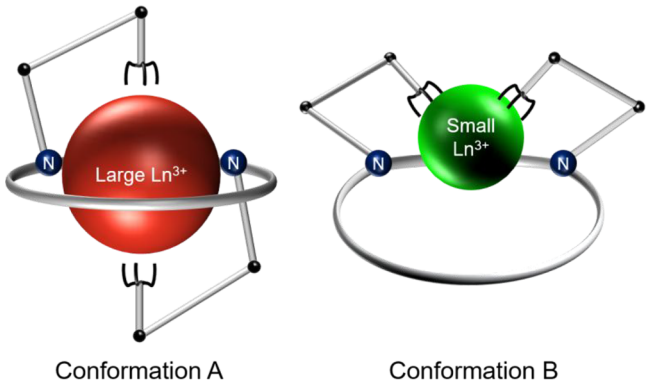

[a]Reproduced from *J. Am. Chem. Soc.* 2020, *142*, 13500. Copyright 2020 American Chemical Society.

radiometal ions including $^{132/135}La^{3+}$ and $^{225}Ac^{3+}$.[13−15] A potential shortcoming of macropa for its broader use in nuclear medicine, however, is its poor affinity and stability in binding smaller ions, a feature that renders it incompatible with medicinally relevant radiometals of this type. Consequently, chelators that are capable of stably holding radionuclides of disparate sizes would be of significant value for use in nuclear medicine.

We recently reported a macrocyclic chelator macrodipa (Chart 1) that shows an unprecedented selectivity pattern for the Ln^{3+} ions by exhibiting good affinities for both the largest and smallest members of this series.[16] This dual-size-selectivity pattern arises from a significant conformational toggle of this chelator that enables it to accommodate Ln^{3+} ions of different sizes, as depicted in Scheme 1. For the large Ln^{3+}, a 10-coordinate, nearly C_2-symmetric complex is formed (Conformation A), whereas for the small Ln^{3+}, an 8-coordinate asymmetric complex arises (Conformation B). We believe that this concept of conformational switching upon coordinating metal ions with different sizes potentially prompts the development of a new class of chelators for nuclear medicine that can accommodate a wide range of radionuclides with disparate chemical properties.

Despite this promising and potentially valuable selectivity pattern of macrodipa, its coordination compounds with Ln^{3+} are kinetically labile (vide infra), a property that limits its use in nuclear medicine. To overcome this shortcoming, we considered different design strategies to enhance the overall thermodynamic and kinetic stability of macrodipa, while maintaining its unusual selectivity pattern. To achieve this goal, we targeted the ligand py-macrodipa (Scheme 1), an "upgraded macrodipa" with one of the ethereal oxygen donors replaced by a pyridyl nitrogen donor. We anticipated that the pyridyl nitrogen donor would enhance both the thermodynamic and kinetic stability of macrodipa. The pyridyl nitrogen donor is a stronger donor for coordinating Ln^{3+} compared to the ethereal oxygen. For instance, in comparing the ligands Oxyaapa and pypa, which differ only by the substitution of an ethereal oxygen donor for a pyridyl donor (Chart 1), the latter forms thermodynamically more stable complexes with Ln^{3+}.[17,18] Furthermore, the planar pyridyl unit is likely to rigidify the metal complex and reinforce its kinetic stability. The incorporation of rigidifying groups into ligand backbones is an established means of enhancing metal complex kinetic inertness,[19] as exemplified by comparing the highly efficacious chelator CHX-A″-DTPA, which contains a rigid *trans*-cyclohexyl ring, to its more flexible analogue DTPA.[10]

Herein, we report the synthesis and characterization of the "upgraded macrodipa" ligand, py-macrodipa. Its coordination chemistry with all 14 nonradioactive Ln^{3+} ions and Sc^{3+}, a class of metals ions that have similar chemical properties but different ionic radii,[20−22] was investigated, enabling us to understand how py-macrodipa interacts with ions of different sizes.[23] The candidacy of py-macrodipa for nuclear medicine applications was also evaluated in this work, demonstrated via radiolabeling studies with ^{135}La and ^{44}Sc radionuclides, two radiometals with significantly different ionic radii that attain the large and small size extremes within the Ln^{3+} series. Through these experiments, we show that py-macrodipa is capable of chelating large ions like La^{3+} and small ions like Sc^{3+} with both satisfactory thermodynamic and kinetics stabilities, marking a significant improvement over macrodipa, our first-

https://doi.org/10.1021/jacs.1c05339
J. Am. Chem. Soc. 2021, 143, 10429−10440

Scheme 2. Synthetic Route to Py-Macrodipa

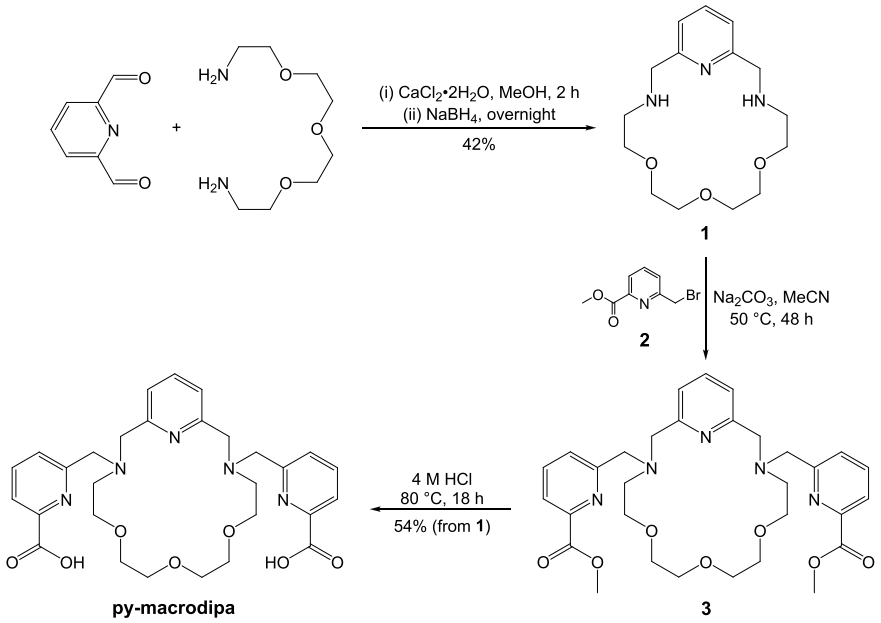

generation "macrodipa-type" ligand. This discovery indicates that py-macrodipa has great potential for use in chelating radiometals with significant size differences, enabling it to be employed with size-mismatched theragnostic pairs.

RESULTS AND DISCUSSION

Ligand Syntheses. The synthesis of py-macrodipa (Scheme 2) involves the assembly of the previously reported macrocyclic core through a reductive animation[24] and the subsequent installation of the two picolinate pendent arms, with an overall yield of 23% over three steps. The identity and purity of the intermediates and final product were ascertained by NMR spectroscopy, mass spectrometry, and analytical HPLC (Figures S1−S9). The macrodipa ligand was obtained via published procedures.[16,25,26]

Ln^{3+} Complex Stability Constants. Metal complex stability constants provide a quantitative measure of the thermodynamic affinity of ligands for metal ions. The magnitudes of these stability constants for various ligands are valuable for assessing their use in different metal chelation applications.[27,28] In order to study the influence of the newly introduced pyridyl group in the macrocycle of py-macrodipa, we determined the protonation constants (K_i, Table S1) of py-macrodipa, as well as the stability constants (K_{LnL}, Table 1) of its Ln^{3+} complexes, via either potentiometric titrations or UV−Vis spectrophotometric titrations.[29−31] These values for macrodipa, which we previously reported[16] except for the newly measured stability constant for Sc^{3+}, are also compared in Tables 1 and S1. These quantities are defined in eqs 1−2, where the concentration terms represent those at chemical equilibrium, and L signifies the uncomplexed ligand in its fully deprotonated state.

$$K_i = [H_iL]/[H^+][H_{i-1}L] \quad (1)$$

$$K_{LnL} = [LnL]/[Ln^{3+}][L] \quad (2)$$

Figure 1 plots log K_{LnL} values against the Ln^{3+} 6-coordinate ionic radius[22] for py-macrodipa and macrodipa. Similar to macrodipa, py-macrodipa shows a dual-size selectivity across the Ln^{3+} series, as reflected by its greater affinity for the large and small ions over the intermediately sized ions. This result demonstrates that the incorporation of the pyridine within the macrocycle does not alter the unique size-selectivity profile and further suggests that py-macrodipa is similarly undergoing a conformational toggle upon traversing the Ln^{3+} series. Remarkably, py-macrodipa shows an overall enhancement in its thermodynamic affinity for the entirety of the Ln^{3+} series compared to macrodipa. For the large Ln^{3+} ions, py-macrodipa exhibits an approximate 2-log-unit increase in K_{LnL} over macrodipa, whereas a 1-log-unit enhancement in stability is observed for the small Ln^{3+}.

The presence of the pyridyl donor in py-macrodipa thus improves the overall Ln^{3+}-binding affinity, while maintaining the novel dual-size-selectivity pattern. Although the K_{LnL} values

Table 1. Stability Constants of the Ln^{3+} Complexes Formed with Py-Macrodipa, Macrodipa, and Macropa

	py-macrodipa[a]	macrodipa[b]	macropa[c]
Ln^{3+}	log K_{LnL}	log K_{LnL}	log K_{LnL}
La^{3+}	14.31(6)	12.19	14.99
Ce^{3+}	14.65(8)	12.50	15.11
Pr^{3+}	14.81(6)	12.41	14.70
Nd^{3+}	14.51(7)	12.25	14.36
Sm^{3+}	13.66(4)	11.52	13.80
Eu^{3+}	13.29(6)	10.93	13.01
Gd^{3+}	12.63(5)	10.23	13.02
Tb^{3+}	11.95(3)	9.68	11.79
Dy^{3+}	11.47(4)	9.36	11.72
Ho^{3+}	10.69(1)	9.36	10.59
Er^{3+}	10.60(3)	9.71	10.10
Tm^{3+}	10.92(2)	10.13	9.59
Yb^{3+}	11.31(4)	10.48	8.89
Lu^{3+}	11.54(2)	10.64	8.25
Sc^{3+}	15.83(2)	14.37(7)	

[a]0.1 M KCl, this work. The values in the parentheses are one standard deviation of the last significant figure. [b]0.1 M KCl. For La^{3+}−Lu^{3+}, ref 16. For Sc^{3+}, this work. [c]0.1 M KCl, ref 12.

https://doi.org/10.1021/jacs.1c05339
J. Am. Chem. Soc. 2021, 143, 10429−10440

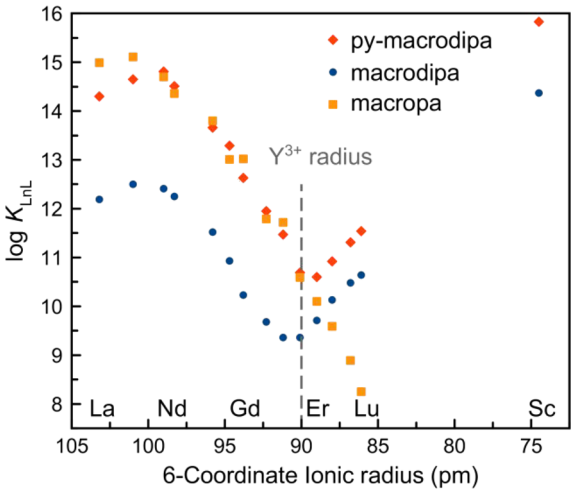

Figure 1. Stability constants of Ln^{3+} complexes formed with py-macrodipa and macrodipa plotted versus ionic radii.

of py-macrodipa are several orders of magnitude smaller than those of the conventional chelating agent DOTA,[32] for the large Ln^{3+} ions, they compare favorably to those of macropa (Figure 1), which has been successfully applied in nuclear medicine applications for radiometals of this type.[13,14] A key advantage of py-macrodipa over macropa, however, is that it retains high affinity for the small Ln^{3+} ions for which macropa is an ineffective chelator.

Complex Structures—NMR Spectroscopy. To investigate the inferred switch between Conformations A and B in py-macrodipa across the Ln^{3+} series, we used NMR spectroscopy to characterize the solution structures of its complexes with the diamagnetic La^{3+}, Lu^{3+}, Sc^{3+}, and Y^{3+} ions, with ionic radii spanning from 103.2 to 74.5 pm. The 90-pm ionic radius[22] of Y^{3+} aligns well with the minimum affinity among all Ln^{3+} complexes (Figure 1). Thus, an investigation of the coordination chemistry of Y^{3+}–py-macrodipa provides insight on the conformational change that is likely occurring as this minimum of stability is traversed.

The ^{1}H and $^{13}C\{^{1}H\}$ NMR spectra of these four complexes were acquired in D_2O at pD 7 (Figures 2 and S28–S35). A gradual change of the complex conformation is observed as the Ln^{3+} gets smaller. For La^{3+}–py-macrodipa, the complex is present as the symmetric Conformation A, whereas the complexes of smaller Lu^{3+} and Sc^{3+} exist solely as the asymmetric Conformation B. The complex of the intermediately sized Y^{3+} ion shows a mixture of both Conformations A and B in a molar ratio of 3.6:1. These conformation are identified and assigned based on our previous detailed multinuclear NMR studies on the La^{3+}, Y^{3+}, and Lu^{3+} complexes of macrodipa.[16] Considering the relatively large difference in ionic radius between La^{3+} and Y^{3+}, we obtained the ^{1}H NMR spectrum of the py-macrodipa complex formed with paramagnetic Eu^{3+} (ionic radius = 94.7 pm).[22] The clearly resolved paramagnetic ^{1}H NMR spectrum of this complex (Figure S36) shows that it adopts the symmetric Conformation A. In this study, we also acquired the ^{1}H and $^{13}C\{^{1}H\}$ spectra of the Sc^{3+}–macrodipa complex (Figures S37–S38), which reveal it to attain Conformation B, as expected based on the small ionic radius of Sc^{3+}. Collectively, these NMR spectroscopic results show that the inclusion of a pyridyl moiety within py-macrodipa does not alter the conformational toggle responsible for accommodating both large and small Ln^{3+} ions that is observed for macrodipa. Consistent with our expectations and prior studies with macrodipa, large Ln^{3+} ions

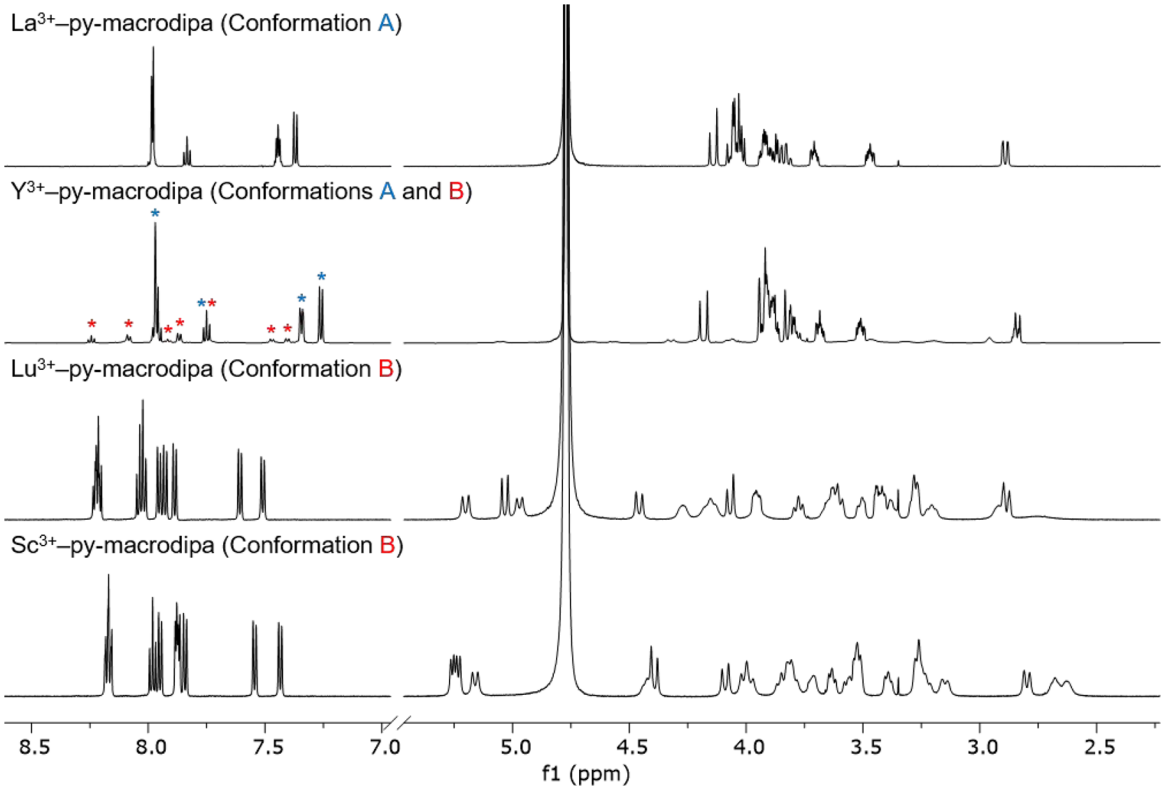

Figure 2. ^{1}H NMR spectra of La^{3+}–, Y^{3+}–, Lu^{3+}–, and Sc^{3+}–py-macrodipa complexes (600 MHz, D_2O, pD 7, 25 °C).

https://doi.org/10.1021/jacs.1c05339
J. Am. Chem. Soc. 2021, 143, 10429–10440

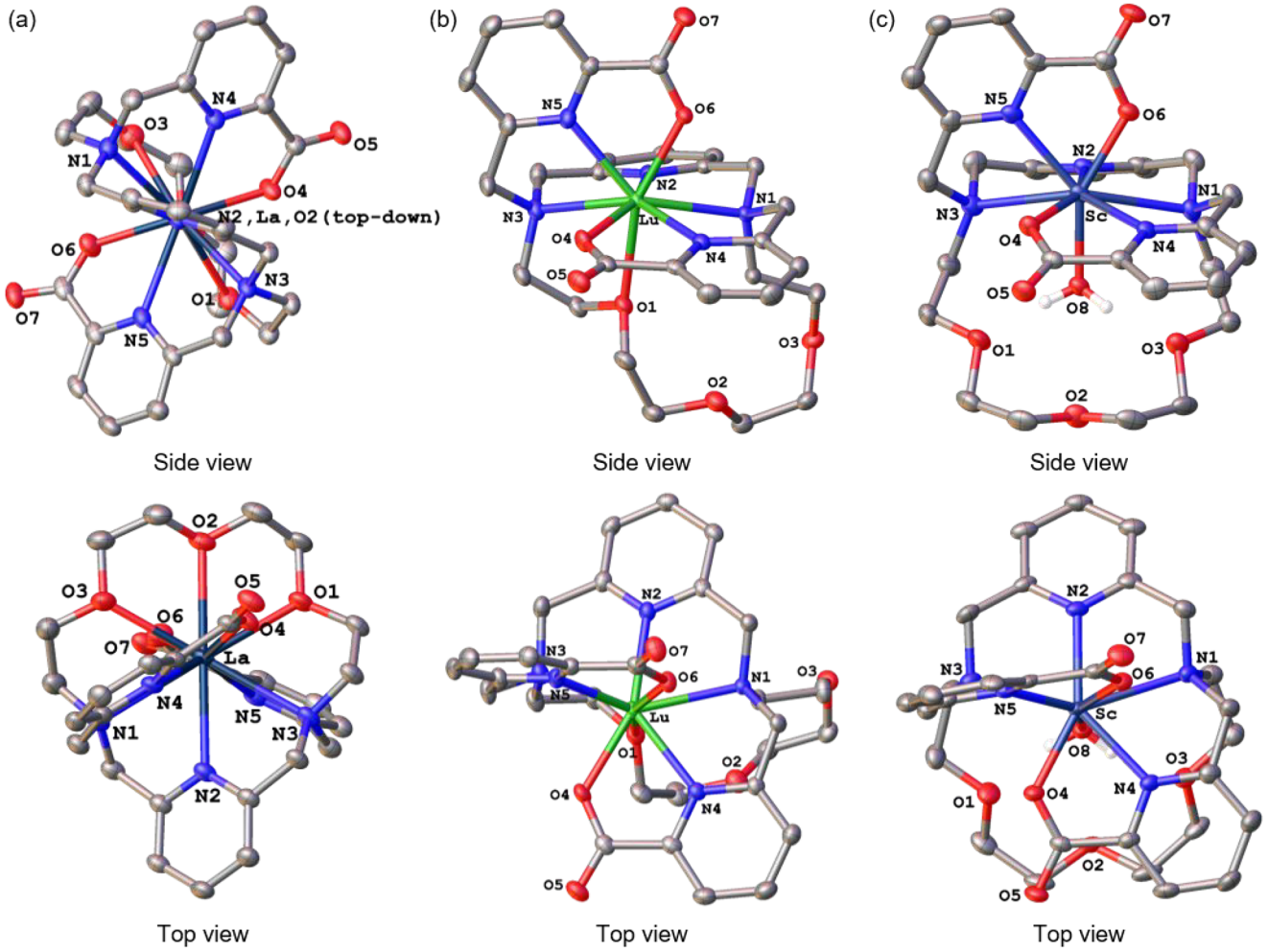

Figure 3. Crystal structures of (a) $[La(py\text{-}macrodipa)]^+$, (b) $[Lu(py\text{-}macrodipa)]^+$, and (c) $[Sc(py\text{-}macrodipa)(OH_2)]^+$ complexes. Thermal ellipsoids are drawn at the 50% probability level. Solvent, counterions, and nonacidic hydrogen atoms are omitted for clarity. Only one of the two $[La(py\text{-}macrodipa)]^+$ or $[Sc(py\text{-}macrodipa)(OH_2)]^+$ complexes in the asymmetric unit is shown.

form symmetric complexes that attain Conformation A, whereas the asymmetric Conformation B is preferred for small Ln^{3+} ions.

Complex Structures—X-ray Crystallography. To gain further insight on the conformational toggle of py-macrodipa across the Ln^{3+} series, we characterized the La^{3+}, Lu^{3+}, and Sc^{3+} complexes by X-ray crystallography. Crystal structures of these three complexes are shown in Figure 3. These crystal structures are consistent with the NMR spectroscopic data, which show the presence of different conformations for Ln^{3+} ions of different sizes. As previously observed for macrodipa, the La^{3+} center in the py-macrodipa complex attains a 10-coordinate geometry, forming a compound with the Conformation A geometry and a slightly distorted C_2 symmetry. For this complex, the central La^{3+} ion is fully encapsulated in the macrocycle, interacting with all of these donors. The two pendent picolinate arms coordinate La^{3+} from above and below the plane of the macrocycle. The complexes of the smaller ions, Lu^{3+} and Sc^{3+}, attain the 8-coordinate Conformation B, which is of low symmetry. In Conformation B, in addition to the two picolinate donor arms, only three of the macrocyclic donors, N1−N3, appreciably interact with the metal centers. Furthermore, the Lu^{3+} and Sc^{3+} complexes are highly comparable except for presence of an inner-sphere water molecule in the Sc^{3+} complex that is absent in the Lu^{3+} complex. With this inner-sphere water molecule, the Sc^{3+}−py-macrodipa complex is consistent with what was previously observed for the Lu^{3+}−macrodipa complex,[16] with both structures showing hydrogen-bonding interactions between the inner-sphere water and the macrocycle ethers. By contrast, the coordination sphere of the Lu^{3+} center in the py-macrodipa complex is completed by one of the ethereal oxygens on the macrocycle in place of the inner-sphere water. Although we consider both Sc^{3+} and Lu^{3+} complexes to attain Conformation B, we distinguish them further by referring to the nonhydrated complex as "Conformation B0" and the complex with the inner-sphere water molecule to be "Conformation B1".

The presence of the inner-sphere water molecule may be a consequence of the conditions under which these crystals were obtained. Crystals of Lu^{3+}−py-macrodipa were grown from the vapor diffusion of Et_2O into a MeOH solution containing the complex, reflecting a situation with a limited H_2O content. By contrast, crystals of Sc^{3+}−py-macrodipa were obtained directly from an aqueous solution, a condition that would most likely favor H_2O coordination. Moreover, the previously reported Lu^{3+}−macrodipa structure, which also attains Conformation B1, was afforded via the analysis of crystals grown from an aqueous solution as well.[16] A recent survey on interatomic distances (r) found within the crystal structures in the Inorganic Crystal Structure Database (ICSD) of Ln^{3+}

https://doi.org/10.1021/jacs.1c05339
J. Am. Chem. Soc. 2021, 143, 10429−10440

complexes with direct oxygen atom coordination revealed an average value of r(Lu−O) = 2.342 ± 0.103 Å for 8-coordinate Lu^{3+} complexes.[33] The distance between the Lu^{3+} center and ethereal oxygen donor O1 within $[Lu(py\text{-}macrodipa)]^+$, r(Lu−O) = 2.509 Å, is substantially longer than the majority of Lu^{3+}−O interactions in the ICSD, suggesting this interaction to be weak. Furthermore, for $[Lu(macrodipa)(OH_2)]^+$, the distance between Lu^{3+} and the bound OH_2 is r(Lu−O) = 2.281 Å, indicating a typical coordination interaction between these two species. On the basis of these findings, we anticipate that in aqueous solution, which is of the most significant relevance to the potential application of this chelator for nuclear medicine, the hydrated Conformation B1 is the dominant species.

DFT Calculations. To further understand the conformational toggle of py-macrodipa across the Ln^{3+} series, as well as the origin of the enhanced thermodynamic stability of Ln^{3+}−py-macrodipa complexes compared to those of Ln^{3+}−macrodipa, we carried out DFT calculations with *Gaussian 09*.[34] For comparative purposes, the same theoretical methods that we had previously implemented for Ln^{3+}−macrodipa (Ln = La−Lu)[16] were applied to study Ln^{3+}−py-macrodipa. Specifically, the dispersion-corrected hybrid functional ωB97XD was employed.[35,36] A large-core relativistic effective core potential (LCRECP) and the associated basis set was assigned to the Ln^{3+} ions (Ln = La−Lu),[37] whereas the 6-31G(d,p) basis set was applied to all other lighter atoms.[38,39] Solvation effects in water were accounted for using the SMD solvation model.[40,41] Furthermore, we also probed Sc^{3+}−macrodipa in this work to compare it directly to its py-macrodipa analogue. A detailed set of equations describing our computational thought flow is given in the Supporting Information.

To investigate the thermodynamic preferences for Conformations A and B for all Ln^{3+}−py-macrodipa complexes, these structures were optimized, and their standard free energies ($G°$) were calculated. Due to our observations of both the nonhydrated and hydrated Conformations B0 and B1 by X-ray crystallography, both structures were calculated. Balanced chemical reactions for the conformational switch between Conformations A and B (B0 or B1) in aqueous solution can be written as either eq 3 or 4, where the standard free energy change of these two reactions are annotated as $\Delta G°$(A,B0) and $\Delta G°$(A,B1), respectively.

$$[Ln(py\text{-}macrodipa)]^+(\text{Conformation A}, aq) \rightleftharpoons [Ln(py\text{-}macrodipa)]^+(\text{Conformation B0}, aq) \quad (3)$$

$$[Ln(py\text{-}macrodipa)]^+(\text{Conformation A}, aq) + H_2O(l) \rightleftharpoons [Ln(py\text{-}macrodipa)]^+(\text{Conformation B1}, aq) \quad (4)$$

Figure 4a summarizes computed $\Delta G°$(A,B0) and $\Delta G°$(A,B1) values across all Ln^{3+}. As expected from the NMR and X-ray crystallographic data, these $\Delta G°$ values are positive for early Ln^{3+} ions, but negative for late Ln^{3+} ions, signifying a change in thermodynamic preference from Conformation A to B as the series is traversed. Additionally, the $\Delta G°$(A,B1) values are systematically more negative than those for $\Delta G°$(A,B0) by ∼30 kJ·mol^{-1}, suggesting that Conformation B1 is considerably more stable than B0 in aqueous solution. Thus, regarding Conformation B, our subsequent calculations focused primarily on Conformation B1.

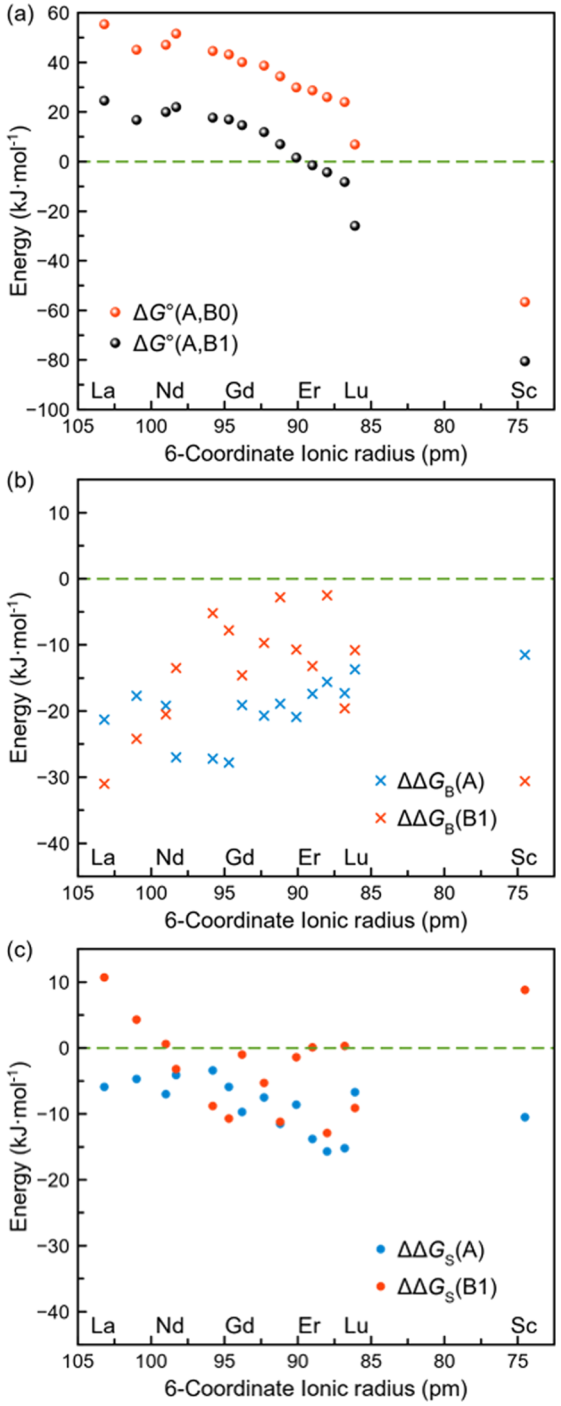

Figure 4. (a) DFT-computed standard free energy differences between Conformations A and B for Ln^{3+}−py-macrodipa complexes, $\Delta G°$(A,B0) and $\Delta G°$(A,B1), as defined in eqs 3, 4. DFT-computed (b) relative binding energies ($\Delta\Delta G_B°$, eq 6) and (c) relative strain energies ($\Delta\Delta G_S°$, eq 7), comparing the Ln^{3+}−py-macrodipa and Ln^{3+}−macrodipa complexes.

Another feature of the Ln^{3+}−py-macrodipa complexes that warrants computational investigation is their enhanced thermodynamic stabilities over the Ln^{3+}−macrodipa complexes. To understand this property, we analyzed the free energy of the formation of these metal−ligand coordination complexes by breaking this process up into two distinct steps. In the first step, the free ligand adjusts its structure to a conformation that is appropriate for metal binding (eq 5), the

https://doi.org/10.1021/jacs.1c05339
J. Am. Chem. Soc. 2021, 143, 10429−10440

free energy change of which is defined as the strain energy (ΔG_S°). Once the ligand has adopted the proper conformation, Ln^{3+} binding occurs (eq 6), resulting in a free energy change defined as the binding energy (ΔG_B°).

$$L^{2-}(\text{free}, aq) \rightleftharpoons L^{2-}(\text{Conformation A or B1}, aq) \quad (5)$$

$$L^{2-}(\text{Conformation A or B1}, aq) + Ln^{3+}(aq) \rightleftharpoons [LnL]^{+}(\text{Conformation A or B1}, aq) \quad (6)$$

These free energy terms, ΔG_S° and ΔG_B°, were investigated for both ligand systems in both possible conformations (A and B1). These values are plotted in a relative manner ($\Delta\Delta G_S^\circ$ and $\Delta\Delta G_B^\circ$, defined in eqs 7, 8) for a straightforward comparison between the two ligand systems, as shown in Figure 4b,c.

$$\Delta\Delta G_S^\circ(\text{A or B1}) = \Delta G_S^\circ(\text{py-macrodipa, A or B1}) - \Delta G_S^\circ(\text{macrodipa, A or B1}) \quad (7)$$

$$\Delta\Delta G_B^\circ(\text{A or B1}) = \Delta G_B^\circ(\text{py-macrodipa, A or B1}) - \Delta G_B^\circ(\text{macrodipa, A or B1}) \quad (8)$$

The difference in binding energies, $\Delta\Delta G_B^\circ$, demonstrates a clear contribution to the enhanced stability of Ln^{3+}–py-macrodipa complexes. Regardless of the complex conformation, both $\Delta\Delta G_B^\circ$(A) and $\Delta\Delta G_B^\circ$(B1) are negative across the whole Ln^{3+} series, indicating that Ln^{3+}-binding is more favorable for py-macrodipa. This result can be attributed to the presence of the pyridyl group within the macrocycle of this ligand, which is a stronger donor than the analogous ethereal oxygen donor in macrodipa. The $\Delta\Delta G_S^\circ$(A) values are less than zero for all Ln^{3+}, indicating that the rigid planar pyridine group in the macrocycle of py-macrodipa favors the complex formation by preorganizing this ligand for metal binding in Conformation A. By contrast, $\Delta\Delta G_S^\circ$(B1) fluctuates about zero across the Ln^{3+} series, suggesting that the rigidity introduced by the pyridyl moiety in py-macrodipa does not significantly influence the complex formation in Conformation B1.

Photophysical Studies. Within the Ln^{3+} series, Eu^{3+} and Tb^{3+} are known for their rich photoluminescent properties.[42−45] For a better understanding and more complete characterization of the Ln^{3+}–py-macrodipa complexes, the photophysical properties of its Eu^{3+} and Tb^{3+} complexes were investigated. These results are summarized in Table 2.

The UV–Vis absorption and emission spectra of these two complexes were acquired at pH 7.4 (Figure S42). Both complexes give rise to an absorption band centered at 273 nm, which is attributed to the $\pi \rightarrow \pi^*$ transition of the pyridyl units.[46] Upon this pyridyl-based excitation, both complexes show characteristic Ln^{3+}-based f-f emissions, through the well-established antenna effect.[47,48] Additionally, we determined their photoluminescence quantum yields by a relative method,[49] using $[Ru(bpy)_3]Cl_2$ (quantum yield = 4.0% in air-saturated water)[50] as the reference compound.

A comparison between luminescence lifetimes (τ) of Eu^{3+} and Tb^{3+} complexes acquired in H_2O and D_2O can be used to determine the number of inner-sphere water molecules (q).[51] The q values of Eu^{3+} and Tb^{3+} complexes are calculated by empirically derived expressions, eqs 9 and 10,[52,53] where $\Delta k_{obs} = 1/\tau(H_2O) - 1/\tau(D_2O)$ in ms^{-1}.

$$q_{Eu} = 1.11 \times (\Delta k_{obs} - 0.31) \quad (9)$$

$$q_{Tb} = 5.0 \times (\Delta k_{obs} - 0.06) \quad (10)$$

As shown in Table 2, the measured τ values in H_2O and D_2O indicate both complexes do not possess any inner-sphere water molecules ($q = 0$). This observation is consistent with our other experimental (Figures 1 and S36) and computational (Figure 4a) results that suggest these complexes adopt Conformation A, where an inner-sphere water is absent.

DTPA Transchelation Challenge Assays. For nuclear medicine applications, the kinetic stabilities of radiometal complexes are of critical importance because release of free metal ions is expected to give rise to toxic side effects.[1] To assess the suitability of py-macrodipa for use in nuclear medicine, we evaluated the kinetic stabilities of the Ln^{3+}–py-macrodipa complexes and compared them to the corresponding Ln^{3+}–macrodipa complexes. Specifically, we monitored the transchelation reaction of these Ln^{3+} complexes by UV–Vis spectroscopy in the presence of 100-fold excess DTPA at pH 7.4 and RT (22 °C), conditions that thermodynamically favor loss of the Ln^{3+} ion from both py-macrodipa and macrodipa.[54−56] With the large excess of DTPA, this reaction follows pseudo-first-order kinetics, enabling us to use readily determined half-lives ($t_{1/2}$) as a comparative measure of the complex kinetic stability. These $t_{1/2}$ values are listed in Table 3.

Table 2. Photophysical Properties of Eu^{3+}– and Tb^{3+}–py-macrodipa Complexes[a]

	λ_{max}/nm	Quantum Yield/%	$\tau(H_2O)$/ms	$\tau(D_2O)$/ms	q
Eu^{3+}–py-macrodipa	273	0.21(1)	1.12(1)	1.43(1)	−0.1
Tb^{3+}–py-macrodipa	273	0.84(4)	3.14(3)	3.14(2)	−0.3

[a]pH 7.4, 22 °C. The values in the parentheses are one standard deviation of the last significant figure.

Table 3. Half-lives of Ln^{3+}–py-macrodipa and Ln^{3+}–macrodipa Complexes when Challenged with 100 Equivalents of DTPA[a]

	Ln^{3+}–py-macrodipa	Ln^{3+}–macrodipa
La^{3+}	6.3 ± 0.3 d	1678 ± 33 s
Nd^{3+}	3.9 ± 0.2 d	615 ± 14 s
Gd^{3+}	5524 ± 107 s	54 ± 2 s
Er^{3+}	578 ± 23 s; 61 ± 3 s	5 ± 1 s
Lu^{3+}	853 ± 10 s	65 ± 1 s
Sc^{3+}	16.6 ± 1.7 h	782 ± 18 s

[a][LnL] = 100 μM, pH 7.4, 22 °C.

For both ligand systems, the kinetic stability of their Ln^{3+} complexes follows the trends of their thermodynamic stability, with the early and late Ln^{3+} complexes displaying greater kinetic stability than those in the middle of the 4f series. Notably, the dissociation of Er^{3+}–py-macrodipa complex follows a biexponential function, affording two pseudo-first-order rate constants. We tentatively assign the two kinetic processes to arise from dissociations of the distinct Conformations A and B, which presumably possess different kinetic labilities. The ^1H NMR spectrum of Y^{3+}–py-macrodipa (Figure 2) provides support for this hypothesis, as it clearly shows a mixture of both conformers. On the basis of the

https://doi.org/10.1021/jacs.1c05339
J. Am. Chem. Soc. 2021, 143, 10429−10440

comparable ionic radii of Er^{3+} (89 pm) and Y^{3+} (90 pm),[22] Er^{3+}−py-macrodipa is expected to similarly exist in solution with both conformers, providing an explanation for the two observed kinetic processes.

Overall, the kinetic stabilities of Ln^{3+}−macrodipa complexes are poor, a property that is reflected by the fact that none of their half-lives exceeds 30 min. By contrast, py-macrodipa forms Ln^{3+} complexes with significantly enhanced kinetic stability. In particular, complexes of both the largest La^{3+} ion ($t_{1/2}$ = 6.3 d) and smallest Sc^{3+} ion ($t_{1/2}$ = 16.6 h) show remarkable kinetic stabilities, a prerequisite for using this ligand in nuclear medicine. These complex $t_{1/2}$ values are substantially longer than the physical half-lives of their corresponding medicinally relevant radionuclides like ^{132}La ($t_{1/2}$ = 4.6 h), ^{135}La ($t_{1/2}$ = 18.9 h), and ^{44}Sc ($t_{1/2}$ = 4.0 h).[57,58] The excellent kinetic stability of La^{3+}− and Sc^{3+}−py-macrodipa indicates that py-macrodipa is a promising candidate for chelating radioactive La^{3+} and Sc^{3+}.

Radiolabeling Studies. Having shown that py-macrodipa forms complexes with La^{3+} and Sc^{3+} of both high thermodynamic and kinetic stabilities, we next sought to evaluate its ability to radiolabel medicinally relevant radioisotopes of these ions. The radionuclides $^{135}La^{3+}$ and $^{44}Sc^{3+}$, which have potential applications for Auger electron therapy and positron emission tomography,[59,60] were produced and isolated following our established procedures.[13,61,62] For comparison, radiolabeling studies were also conducted using macrodipa and DOTA. For py-macrodipa and macrodipa, these experiments were executed at 25 °C, whereas for DOTA the elevated temperature of 80 °C was employed due to its known slower binding kinetics. These studies used a pH 5.5 buffer, and the reactions were monitored at 15, 30, and 60 min.

Table 4. Apparent Molar Activity (AMA, Ci·μmol^{-1}) of $^{135}La^{3+}$ and $^{44}Sc^{3+}$ Radiolabeling with Ligands Py-Macrodipa, Macrodipa, and DOTA

	Radiolabeling Conditions		$^{135}La^{3+}$	$^{44}Sc^{3+}$
py-macrodipa	pH 5.5, 25 °C	15 min	1.488	0.798
		30 min	1.363	0.888
		60 min	1.709	0.733
macrodipa	pH 5.5, 25 °C	15 min	0.105	0.006
		30 min	0.088	0.004
		60 min	0.095	0.004
DOTA	pH 5.5, 80 °C	15 min	0.005	0.419
		30 min	0.020	0.395
		60 min	0.030	0.464

Table 4 lists the apparent molar activities (AMA) for the ^{135}La- and ^{44}Sc-labeled ligands obtained under these conditions. AMA, which describes the amount of radionuclide activity incorporated normalized to the amount of chelator, has been previously used to compare the radiolabeling efficacies of different ligands.[13,61−63] Among these three ligands, py-macrodipa affords significantly higher AMAs for both ^{44}Sc and ^{135}La in comparison to the other ligands. Notably, the AMA does not appreciably increase beyond 15 min, indicating that radiolabeling at this mild temperature (25 °C) for this ligand is complete on this short time scale. The AMAs obtained for macrodipa show that although it can bind $^{135}La^{3+}$, it is ineffective for $^{44}Sc^{3+}$. Conversely, even at elevated temperatures, the established chelator DOTA was only able to bind the smaller $^{44}Sc^{3+}$ radionuclide but failed in sufficiently complexing the large $^{135}La^{3+}$ radionuclide.

Collectively, these data show that py-macrodipa exhibits versatile radiolabeling properties, enabling it to effectively bind to both the large $^{135}La^{3+}$ and small $^{44}Sc^{3+}$ radionuclides. Its overall radiolabeling efficiency, as reflected by significantly large AMAs, is substantially better than those of our first-generation ligand macrodipa, thus validating our design strategy of incorporating the pyridyl donor within the macrocycle. In comparison to the widely used "gold-standard" ligand DOTA, py-macrodipa can effectively be radiolabeled by ions of both types. To our best knowledge, py-macrodipa is the first chelator capable of effectively binding both La^{3+} and Sc^{3+} radionuclides, which possess substantially different ionic radii.

Human Serum Challenge Assays. Having demonstrated that py-macrodipa is effectively radiolabeled by $^{135}La^{3+}$ and $^{44}Sc^{3+}$, we next evaluated the kinetic stability of the resulting complexes of these radiometals in human serum at 37 °C to assess the potential value of this ligand for nuclear medicine. The stabilities of $^{135}La^{3+}$− and $^{44}Sc^{3+}$−py-macrodipa complexes were monitored by radio-HPLC over 48 and 8 h, respectively, time periods that account for the different physical half-lives of these radionuclides. Although the signal-to-noise of the chromatograms gradually decreases due to the physical decay of the radionuclides, only a single peak in the chromatograms corresponding to $^{135}La^{3+}$− and $^{44}Sc^{3+}$−py-macrodipa complexes is observed over the duration of experiment (Figure 5a,b), indicating that both complexes exhibit superb kinetic stabilities in human serum. For comparison, the $^{135}La^{3+}$− and $^{44}Sc^{3+}$−macrodipa complexes were also tested for their stabilities in human serum (Figure 5c,d). Although $^{135}La^{3+}$−macrodipa is sufficiently stable in human serum over 48 h, $^{44}Sc^{3+}$−macrodipa complex shows deficient kinetic stability. These results highlight that py-macrodipa is an improvement over macrodipa because of its ability to form kinetically stable complexes with both the large $^{135}La^{3+}$ and small $^{44}Sc^{3+}$. Thus, based on its promising radiolabeling and radiometal-stabilizing properties, py-macrodipa is a valuable radiopharmaceutical candidate.

CONCLUSION

In this work, the ligand py-macrodipa was successfully synthesized and its coordination chemistry with the Ln^{3+} ions was investigated in detail via both experimental and theoretical methods. Building upon the unusual dual-size selectivity of our first-generation ligand macrodipa, we have shown that the presence of the pyridyl moiety within the macrocycle of py-macrodipa substantially improves both the thermodynamic and kinetic stability of its Ln^{3+} complexes. The enhanced Ln^{3+}-binding properties of py-macrodipa manifest in efficient radiolabeling of both $^{135}La^{3+}$ and $^{44}Sc^{3+}$ and excellent stability of the resulting complexes in human serum. This ligand is the first chelator capable of binding radiometal ions with disparate sizes such as $^{135}La^{3+}$ and $^{44}Sc^{3+}$, both with satisfactory efficacy, marking a significant improvement over current state-of-the-art gold standard chelator DOTA, which can only be used for a single type of ion. We thus describe py-macrodipa as a "Janus chelator" because of its ability to effectively bind two types of metal ions by switching its conformation. The success of py-macrodipa demonstrates that coordination chemists can tailor a ligand to effectively bind

https://doi.org/10.1021/jacs.1c05339
J. Am. Chem. Soc. 2021, 143, 10429−10440

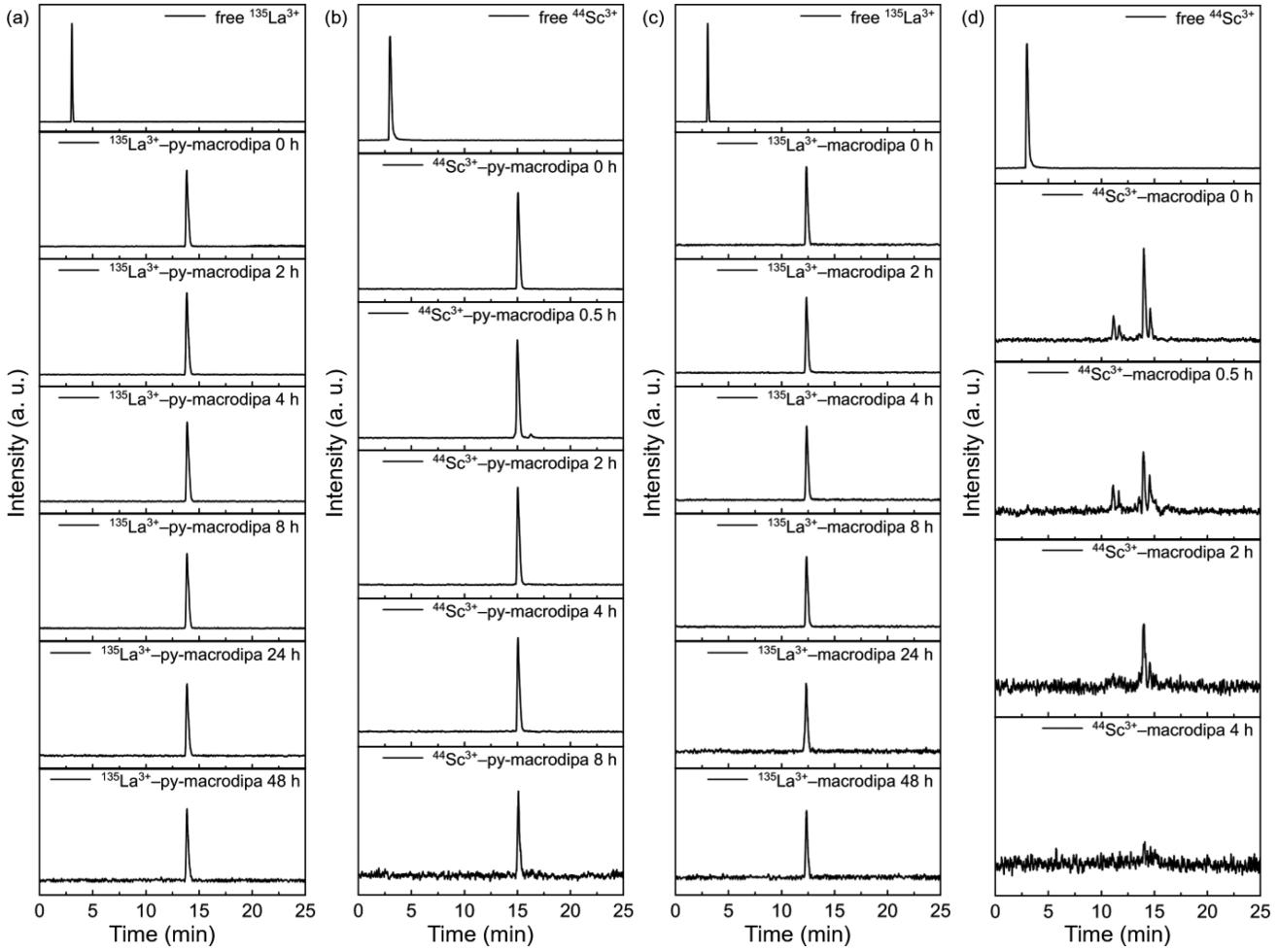

Figure 5. Human serum challenge (37 °C) on the (a) $^{135}La^{3+}$–py-macrodipa, (b) $^{44}Sc^{3+}$–py-macrodipa, (c) $^{135}La^{3+}$–macrodipa, and (d) $^{44}Sc^{3+}$–macrodipa complexes monitored by radio-HPLC.

metal ions with disparate properties, rather than optimizing a ligand for a single ion type. Even though this work focused exclusively on the Ln^{3+} series, we anticipate that this concept can be expanded to other metal ions on the periodic table. Another genre of "Janus chelator" was recently reported, where the chelator switches between phenolate and pyridine pendant donors to effectively bind the Mn ion in both its chemically hard and borderline +3 and +2 oxidation states.[64] Thus, our description of py-macrodipa, as a Janus chelator that bends its backbone differently to accommodate ions of different sizes, provides a complementary approach. The design of py-macrodipa is an important achievement for inspiring future ligand design strategies and represents an important step in realizing an omnipotent "Janus chelator" that can bind all metal ions of disparate properties. Ongoing work is focused on the development and implementation of a bifunctional derivative of py-macrodipa that can be used for targeted nuclear medicine.

■ ASSOCIATED CONTENT

Supporting Information

The Supporting Information is available free of charge at https://pubs.acs.org/doi/10.1021/jacs.1c05339.

Experimental procedures and supplementary data for syntheses, potentiometric titrations, UV–Vis spectrophotometric titrations, NMR spectroscopy studies, X-ray crystallography studies, DFT calculations, photophysical studies, DTPA transchelation challenges, radiolabeling studies, and human serum challenges (PDF)

Geometry outputs for all DFT-optimized structures (ZIP)

Accession Codes

CCDC 2085495–2085497 contain the supplementary crystallographic data for this paper. These data can be obtained free of charge via www.ccdc.cam.ac.uk/data_request/cif, or by emailing data_request@ccdc.cam.ac.uk, or by contacting The Cambridge Crystallographic Data Centre, 12 Union Road, Cambridge CB2 1EZ, UK; fax: + 44 1223 336033.

■ AUTHOR INFORMATION

Corresponding Author

Justin J. Wilson – *Department of Chemistry and Chemical Biology, Cornell University, Ithaca, New York 14853, United States;* orcid.org/0000-0002-4086-7982; Email: jjw275@cornell.edu

Authors

Aohan Hu – *Department of Chemistry and Chemical Biology, Cornell University, Ithaca, New York 14853, United States;* orcid.org/0000-0002-9720-3159

Eduardo Aluicio-Sarduy − *Department of Medical Physics, University of Wisconsin—Madison, Madison, Wisconsin 53706, United States*
Victoria Brown − *Department of Chemistry, Simon Fraser University, Burnaby, British Columbia V5A 1S6, Canada;* orcid.org/0000-0002-0216-3538
Samantha N. MacMillan − *Department of Chemistry and Chemical Biology, Cornell University, Ithaca, New York 14853, United States;* orcid.org/0000-0001-6516-1823
Kaelyn V. Becker − *Department of Medical Physics and Department of Radiology, University of Wisconsin—Madison, Madison, Wisconsin 53706, United States*
Todd E. Barnhart − *Department of Medical Physics, University of Wisconsin—Madison, Madison, Wisconsin 53706, United States*
Valery Radchenko − *Life Sciences Division, TRIUMF, Vancouver, British Columbia V6T 2A3, Canada; Department of Chemistry, University of British Columbia, Vancouver, British Columbia V6T 1Z1, Canada*
Caterina F. Ramogida − *Department of Chemistry, Simon Fraser University, Burnaby, British Columbia V5A 1S6, Canada; Life Sciences Division, TRIUMF, Vancouver, British Columbia V6T 2A3, Canada;* orcid.org/0000-0003-4815-2647
Jonathan W. Engle − *Department of Medical Physics and Department of Radiology, University of Wisconsin—Madison, Madison, Wisconsin 53706, United States;* orcid.org/0000-0002-3399-7228

Complete contact information is available at: https://pubs.acs.org/10.1021/jacs.1c05339

Notes

The authors declare no competing financial interest.

■ ACKNOWLEDGMENTS

This research was supported by the National Institutes of Biomedical Imaging and Bioengineering of the National Institutes of Health under Award Numbers R21EB027282 and R01EB029259. This research made use of the NMR Facility at Cornell University, which is supported, in part, by the U.S. National Science Foundation under award number CHE-1531632. This work was supported in part by award from the Department of Energy Office of Science (DE-SC0020417). TRIUMF receives funding via a contribution agreement with the National Research Council of Canada. We thank Mr. Angus Koller and Prof. Eszter Boros at Stony Brook University for valuable discussions.

■ REFERENCES

(1) *Radiopharmaceutical Chemistry*; Lewis, J. S., Windhorst, A. D., Zeglis, B. M., Eds.; Springer Nature Switzerland AG: Cham, Switzerland, 2019.
(2) Sgouros, G.; Bodei, L.; McDevitt, M. R.; Nedrow, J. R. Radiopharmaceutical Therapy in Cancer: Clinical Advances and Challenges. *Nat. Rev. Drug Discovery* **2020**, *19*, 589−608.
(3) Dondi, M.; Kashyap, R.; Paez, D.; Pascual, T.; Zaknun, J.; Mut Bastos, F.; Pynda, Y. Trends in Nuclear Medicine in Developing Countries. *J. Nucl. Med.* **2011**, *52*, 16S−23S.
(4) Delbeke, D.; Segall, G. M. Status of and Trends in Nuclear Medicine in the United States. *J. Nucl. Med.* **2011**, *52*, 24S−28S.
(5) Blower, P. J. A Nuclear Chocolate Box: the Periodic Table of Nuclear Medicine. *Dalton Trans.* **2015**, *44*, 4819−4844.
(6) Cutler, C. S.; Hennkens, H. M.; Sisay, N.; Huclier-Markai, S.; Jurisson, S. S. Radiometals for Combined Imaging and Therapy. *Chem. Rev.* **2013**, *113*, 858−883.
(7) Boros, E.; Packard, A. B. Radioactive Transition Metals for Imaging and Therapy. *Chem. Rev.* **2019**, *119*, 870−901.
(8) Kostelnik, T. I.; Orvig, C. Radioactive Main Group and Rare Earth Metals for Imaging and Therapy. *Chem. Rev.* **2019**, *119*, 902−956.
(9) Mikolajczak, R.; van der Meulen, N. P.; Lapi, S. E. Radiometals for Imaging and Theranostics, Current Production, and Future Perspectives. *J. Labelled Compd. Radiopharm.* **2019**, *62*, 615−634.
(10) Price, E. W.; Orvig, C. Matching Chelators to Radiometals for Radiopharmaceuticals. *Chem. Soc. Rev.* **2014**, *43*, 260−290.
(11) Stasiuk, G. J.; Long, N. J. The Ubiquitous DOTA and its Derivatives: the Impact of 1,4,7,10-Tetraazacyclododecane-1,4,7,10-tetraacetic Acid on Biomedical Imaging. *Chem. Commun.* **2013**, *49*, 2732−2746.
(12) Roca-Sabio, A.; Mato-Iglesias, M.; Esteban-Gómez, D.; Tóth, É.; de Blas, A.; Platas-Iglesias, C.; Rodríguez-Blas, T. Macrocyclic Receptor Exhibiting Unprecedented Selectivity for Light Lanthanides. *J. Am. Chem. Soc.* **2009**, *131*, 3331−3341.
(13) Aluicio-Sarduy, E.; Thiele, N. A.; Martin, K. E.; Vaughn, B. A.; Devaraj, J.; Olson, A. P.; Barnhart, T. E.; Wilson, J. J.; Boros, E.; Engle, J. W. Establishing Radiolanthanum Chemistry for Targeted Nuclear Medicine Applications. *Chem. - Eur. J.* **2020**, *26*, 1238−1242.
(14) Thiele, N. A.; Brown, V.; Kelly, J. M.; Amor-Coarasa, A.; Jermilova, U.; MacMillan, S. N.; Nikolopoulou, A.; Ponnala, S.; Ramogida, C. F.; Robertson, A. K. H.; Rodríguez-Rodríguez, C.; Schaffer, P.; Williams, C., Jr; Babich, J. W.; Radchenko, V.; Wilson, J. J. An Eighteen-Membered Macrocyclic Ligand for Actinium-225 Targeted Alpha Therapy. *Angew. Chem., Int. Ed.* **2017**, *56*, 14712−14717.
(15) Abou, D. S.; Thiele, N. A.; Gutsche, N. T.; Villmer, A.; Zhang, H.; Woods, J. J.; Baidoo, K. E.; Escorcia, F. E.; Wilson, J. J.; Thorek, D. L. J. Towards the Stable Chelation of Radium for Biomedical Applications with an 18-Membered Macrocyclic Ligand. *Chem. Sci.* **2021**, *12*, 3733−3742.
(16) Hu, A.; MacMillan, S. N.; Wilson, J. J. Macrocyclic Ligands with an Unprecedented Size-Selectivity Pattern for the Lanthanide Ions. *J. Am. Chem. Soc.* **2020**, *142*, 13500−13506.
(17) Hu, A.; Keresztes, I.; MacMillan, S. N.; Yang, Y.; Ding, E.; Zipfel, W. R.; DiStasio, R. A., Jr; Babich, J. W.; Wilson, J. J. Oxyaapa: A Picolinate-Based Ligand with Five Oxygen Donors that Strongly Chelates Lanthanides. *Inorg. Chem.* **2020**, *59*, 5116−5132.
(18) Li, L.; Jaraquemada-Peláez, M. de G.; Kuo, H.-T.; Merkens, H.; Choudhary, N.; Gitschtaler, K.; Jermilova, U.; Colpo, N.; Uribe-Munoz, C.; Radchenko, V.; Schaffer, P.; Lin, K.-S.; Bénard, F.; Orvig, C. Functionally Versatile and Highly Stable Chelator for ^{111}In and ^{177}Lu: Proof-of-Principle Prostate-Specific Membrane Antigen Targeting. *Bioconjugate Chem.* **2019**, *30*, 1539−1553.
(19) Hancock, R. D.; Martell, A. E. Ligand Design for Selective Complexation of Metal Ions in Aqueous Solution. *Chem. Rev.* **1989**, *89*, 1875−1914.
(20) Cotton, S. A. Scandium, Yttrium & the Lanthanides: Inorganic & Coordination Chemistry. *Encyclopedia of Inorganic Chemistry*; John Wiley & Sons, Ltd.: Chichester, UK, 2006.
(21) Seitz, M.; Oliver, A. G.; Raymond, K. N. The Lanthanide Contraction Revisited. *J. Am. Chem. Soc.* **2007**, *129*, 11153−11160.
(22) Shannon, R. D. Revised Effective Ionic Radii and Systematic Studies of Interatomic Distances in Halides and Chalcogenides. *Acta Crystallogr., Sect. A: Found. Adv.* **1976**, *32*, 751−767.
(23) In the following discussion, we will include Sc^{3+} into the term Ln^{3+} (i.e., Ln = La−Lu, Sc) for simplicity, unless otherwise notified.
(24) Lüning, U.; Baumstark, R.; Peters, K.; von Schnering, H. G. Concave Reagents, 3. Synthesis, Basicity, and Conformation of New Concave Pyridines. *Liebigs Ann. Chem.* **1990**, *1990*, 129−143.
(25) Griffin, J. L. W.; Coveney, P. V.; Whiting, A.; Davey, R. Design and Synthesis of Macrocyclic Ligands for Specific Interaction with Crystalline Ettringite and Demonstration of a Viable Mechanism for

the Setting of Cement. *J. Chem. Soc., Perkin Trans. 2* **1999**, 1973−1981.
(26) Lukyanenko, N. G.; Basok, S. S.; Filonova, L. K. Macroheterocycles. Part 44. Facile Synthesis of Azacrown Ethers and Cryptands in a Two-Phase System. *J. Chem. Soc., Perkin Trans. 1* **1988**, 3141−3147.
(27) Martell, A. E.; Hancock, R. D. Stability Constants and Their Measurements. *Metal Complexes in Aqueous Solutions*; Plenum Press: New York, 1996; pp 217−244.
(28) Peters, J. A.; Djanashvili, K.; Geraldes, C. F. G. C.; Platas-Iglesias, C. The Chemical Consequences of the Gradual Decrease of the Ionic Radius along the Ln-Series. *Coord. Chem. Rev.* **2020**, *406*, 213146.
(29) Gans, P.; O'Sullivan, B. GLEE, a New Computer Program for Glass Electrode Calibration. *Talanta* **2000**, *51*, 33−37.
(30) Gans, P.; Sabatini, A.; Vacca, A. Investigation of Equilibria in Solution. Determination of Equilibrium Constants with the HYPERQUAD Suite of Programs. *Talanta* **1996**, *43*, 1739−1753.
(31) Gans, P.; Sabatini, A.; Vacca, A. Determination of Equilibrium Constants from Spectrophometric Data Obtained from Solutions of Known pH: the Program pHab. *Ann. Chim.* **1999**, *89*, 45−49.
(32) Cacheris, W. P.; Nickle, S. K.; Sherry, A. D. Thermodynamic study of Lanthanide Complexes of 1,4,7-Triazacyclononane-*N*,*N*′,*N*″-triacetic Acid and 1,4,7,10-Tetraazacyclododecane-*N*,*N*′,*N*″,*N*‴-tetraacetic Acid. *Inorg. Chem.* **1987**, *26*, 958−960.
(33) Gagné, O. C. Bond-Length Distributions for Ions Bonded to Oxygen: Results for the Lanthanides and Actinides and Discussion of the f-Block Contraction. *Acta Crystallogr., Sect. B: Struct. Sci., Cryst. Eng. Mater.* **2018**, *74*, 49−62.
(34) Frisch, M. J.; Trucks, G. W.; Schlegel, H. B.; Scuseria, G. E.; Robb, M. A.; Cheeseman, J. R.; Scalmani, G.; Barone, V.; Mennucci, B.; Petersson, G. A.; Nakatsuji, H.; Caricato, M.; Li, X.; Hratchian, H. P.; Izmaylov, A. F.; Bloino, J.; Zheng, G.; Sonnenberg, J. L.; Hada, M.; Ehara, M.; Toyota, K.; Fukuda, R.; Hasegawa, J.; Ishida, M.; Nakajima, T.; Honda, Y.; Kitao, O.; Nakai, H.; Vreven, T.; Montgomery, J. A., Jr.; Peralta, J. E.; Ogliaro, F.; Bearpark, M.; Heyd, J. J.; Brothers, E.; Kudin, K. N.; Staroverov, V. N.; Kobayashi, R.; Normand, J.; Raghavachari, K.; Rendell, A.; Burant, J. C.; Iyengar, S. S.; Tomasi, J.; Cossi, M.; Rega, N.; Millam, J. M.; Klene, M.; Knox, J. E.; Cross, J. B.; Bakken, V.; Adamo, C.; Jaramillo, J.; Gomperts, R.; Stratmann, R. E.; Yazyev, O.; Austin, A. J.; Cammi, R.; Pomelli, C.; Ochterski, J. W.; Martin, R. L.; Morokuma, K.; Zakrzewski, V. G.; Voth, G. A.; Salvador, P.; Dannenberg, J. J.; Dapprich, S.; Daniels, A. D.; Farkas, Ö.; Foresman, J. B.; Ortiz, J. V.; Cioslowski, J.; Fox, D. J. *Gaussian 09*, Revision D. 01; Gaussian, Inc.: Wallingford, CT, 2009.
(35) Chai, J.-D.; Head-Gordon, M. Systematic Optimization of Long-Range Corrected Hybrid Density Functionals. *J. Chem. Phys.* **2008**, *128*, 084106.
(36) Chai, J.-D.; Head-Gordon, M. Long-Range Corrected Hybrid Density Functionals with Damped Atom-Atom Dispersion Corrections. *Phys. Chem. Chem. Phys.* **2008**, *10*, 6615−6620.
(37) Dolg, M.; Stoll, H.; Savin, A.; Preuss, H. Energy-Adjusted Pseudopotentials for the Rare Earth Elements. *Theor. Chim. Acta* **1989**, *75*, 173−194.
(38) Hehre, W. J.; Ditchfield, R.; Pople, J. A. Self-Consistent Molecular Orbital Methods. XII. Further Extensions of Gaussian-Type Basis Sets for Use in Molecular Orbital Studies of Organic Molecules. *J. Chem. Phys.* **1972**, *56*, 2257−2261.
(39) Hariharan, P. C.; Pople, J. A. The Influence of Polarization Functions on Molecular Orbital Hydrogenation Energies. *Theor. Chim. Acta* **1973**, *28*, 213−222.
(40) Marenich, A. V.; Cramer, C. J.; Truhlar, D. G. Universal Solvation Model Based on Solute Electron Density and on a Continuum Model of the Solvent Defined by the Bulk Dielectric Constant and Atomic Surface Tensions. *J. Phys. Chem. B* **2009**, *113*, 6378−6396.
(41) Regueiro-Figueroa, M.; Esteban-Gómez, D.; de Blas, A.; Rodríguez-Blas, T.; Platas-Iglesias, C. Understanding Stability Trends along the Lanthanide Series. *Chem. - Eur. J.* **2014**, *20*, 3974−3981.
(42) Parker, D.; Dickins, R. S.; Puschmann, H.; Crossland, C.; Howard, J. A. K. Being Excited by Lanthanide Coordination Complexes: Aqua Species, Chirality, Excited-State Chemistry, and Exchange Dynamics. *Chem. Rev.* **2002**, *102*, 1977−2010.
(43) Bünzli, J.-C. G. Lanthanide Luminescence for Biomedical Analyses and Imaging. *Chem. Rev.* **2010**, *110*, 2729−2755.
(44) Heffern, M. C.; Matosziuk, L. M.; Meade, T. J. Lanthanide Probes for Bioresponsive Imaging. *Chem. Rev.* **2014**, *114*, 4496−4539.
(45) Kaczmarek, M. Lanthanide-Sensitized Luminescence and Chemiluminescence in the Systems Containing Most Often Used Medicines; A Review. *J. Lumin.* **2020**, *222*, 117174.
(46) Chatterton, N.; Bretonnière, Y.; Pécaut, J.; Mazzanti, M. An Efficient Design for the Rigid Assembly of Four Bidentate Chromophores in Water-Stable Highly Luminescent Lanthanide Complexes. *Angew. Chem., Int. Ed.* **2005**, *44*, 7595−7598.
(47) Moore, E. G.; Samuel, A. P. S.; Raymond, K. N. From Antenna to Assay: Lessons Learned in Lanthanide Luminescence. *Acc. Chem. Res.* **2009**, *42*, 542−552.
(48) Armelao, L.; Quici, S.; Barigelletti, F.; Accorsi, G.; Bottaro, G.; Cavazzini, M.; Tondello, E. Design of Luminescent Lanthanide Complexes: From Molecules to Highly Efficient Photo-Emitting Materials. *Coord. Chem. Rev.* **2010**, *254*, 487−505.
(49) Brouwer, A. M. Standards for Photoluminescence Quantum Yield Measurements in Solution (IUPAC Technical Report). *Pure Appl. Chem.* **2011**, *83*, 2213−2228.
(50) Suzuki, K.; Kobayashi, A.; Kaneko, S.; Takehira, K.; Yoshihara, T.; Ishida, H.; Shiina, Y.; Oishi, S.; Tobita, S. Reevaluation of Absolute Luminescence Quantum Yields of Standard Solutions Using a Spectrometer with an Integrating Sphere and a Back-Thinned CCD Detector. *Phys. Chem. Chem. Phys.* **2009**, *11*, 9850−9860.
(51) Horrocks, W. DeW., Jr; Sudnick, D. R. Lanthanide Ion Probes of Structure in Biology. Laser-Induced Luminescence Decay Constants Provide a Direct Measure of the Number of Metal-Coordinated Water Molecules. *J. Am. Chem. Soc.* **1979**, *101*, 334−340.
(52) Supkowski, R. M.; Horrocks, W. DeW., Jr. On the Determination of the Number of Water Molecules, *q*, Coordinated to Europium(III) Ions in Solution from Luminescence Decay Lifetimes. *Inorg. Chim. Acta* **2002**, *340*, 44−48.
(53) Beeby, A.; Clarkson, I. M.; Dickins, R. S.; Faulkner, S.; Parker, D.; Royle, L.; de Sousa, A. S.; Williams, J. A. G.; Woods, M. Non-Radiative Deactivation of the Excited States of Europium, Terbium and Ytterbium Complexes by Proximate Energy-Matched OH, NH and CH Oscillators: An Improved Luminescence Method for Establishing Solution Hydration States. *J. Chem. Soc., Perkin Trans. 2* **1999**, 493−503.
(54) Grimes, T. S.; Nash, K. L. Acid Dissociation Constants and Rare Earth Stability Constants for DTPA. *J. Solution Chem.* **2014**, *43*, 298−313.
(55) Moeller, T.; Thompson, L. C. Observations on the Rare Earths—LXXV: The Stabilities of Diethylenetriaminepentaacetic Acid Chelates. *J. Inorg. Nucl. Chem.* **1962**, *24*, 499−510.
(56) Pniok, M.; Kubíček, V.; Havlíčková, J.; Kotek, J.; Sabatie-Gogová, A.; Plutnar, J.; Huclier-Markai, S.; Hermann, P. Thermodynamic and Kinetic Study of Scandium(III) Complexes of DTPA and DOTA: A Step Toward Scandium Radiopharmaceuticals. *Chem. - Eur. J.* **2014**, *20*, 7944−7955.
(57) Abel, E. P.; Clause, H. K.; Fonslet, J.; Nickles, R. J.; Severin, G. W. Half-Lives of ^{132}La and ^{135}La. *Phys. Rev. C* **2018**, *97*, 034312.
(58) García-Toraño, E.; Peyrés, V.; Roteta, M.; Sánchez-Cabezudo, A. I.; Romero, E.; Martínez Ortega, A. Standardisation and Precise Determination of the Half-Life of ^{44}Sc. *Appl. Radiat. Isot.* **2016**, *109*, 314−318.
(59) Fonslet, J.; Lee, B. Q.; Tran, T. A.; Siragusa, M.; Jensen, M.; Kibédi, T.; Stuchbery, A. E.; Severin, G. W. ^{135}La as an Auger-Electron Emitter for Targeted Internal Radiotherapy. *Phys. Med. Biol.* **2018**, *63*, 015026.
(60) Price, T. W.; Greenman, J.; Stasiuk, G. J. Current Advances in Ligand Design for Inorganic Positron Emission Tomography Tracers ^{68}Ga, ^{64}Cu, ^{89}Zr and ^{44}Sc. *Dalton Trans.* **2016**, *45*, 15702−15724.

https://doi.org/10.1021/jacs.1c05339
J. Am. Chem. Soc. 2021, 143, 10429−10440

(61) Aluicio-Sarduy, E.; Hernandez, R.; Olson, A. P.; Barnhart, T. E.; Cai, W.; Ellison, P. A.; Engle, J. W. Production and *in vivo* PET/CT Imaging of the Theranostic Pair $^{132/135}$La. *Sci. Rep.* **2019**, *9*, 10658.
(62) Vaughn, B. A.; Ahn, S. H.; Aluicio-Sarduy, E.; Devaraj, J.; Olson, A. P.; Engle, J.; Boros, E. Chelation with a Twist: a Bifunctional Chelator to Enable Room Temperature Radiolabeling and Targeted PET Imaging with Scandium-44. *Chem. Sci.* **2020**, *11*, 333−342.
(63) Aluicio-Sarduy, E.; Hernandez, R.; Valdovinos, H. F.; Kutyreff, C. J.; Ellison, P. A.; Barnhart, T. E.; Nickles, R. J.; Engle, J. W. Simplified and Automatable Radiochemical Separation Strategy for the Production of Radiopharmaceutical Quality ^{86}Y Using Single Column Extraction Chromatography. *Appl. Radiat. Isot.* **2018**, *142*, 28−31.
(64) Gale, E. M.; Jones, C. M.; Ramsay, I.; Farrar, C. T.; Caravan, P. A Janus Chelator Enables Biochemically Responsive MRI Contrast with Exceptional Dynamic Range. *J. Am. Chem. Soc.* **2016**, *138*, 15861−15864.

https://doi.org/10.1021/jacs.1c05339
J. Am. Chem. Soc. 2021, 143, 10429−10440